Supporting Information:

Remote doping of scalable nanowire branches

Martin Friedl,[†,⊥] Kris Cerveny,[‡,⊥] Chunyi Huang,[¶] Didem Dede,[†] Mohammad Samani,[‡] Megan O. Hill,[¶] Nicholas Morgan,[†] Wonjong Kim,[†] Lucas Güniat,[†] Jaime Segura-Ruiz,[§] Lincoln J. Lauhon,[¶] Dominik M. Zumbühl,[‡] and Anna Fontcuberta i Morral[*,†,‖]

†*Department of Materials Science and Engineering, École Polytechnique Fédérale de Lausanne, Lausanne, Switzerland*

‡*Department of Physics, University of Basel, Basel, Switzerland*

¶*Department of Materials Science and Engineering, Northwestern University, Evanston, USA*

§*European Synchrotron Radiation Facility, Grenoble, 38043, France*

‖*Department of Physics, École Polytechnique Fédérale de Lausanne, Lausanne, Switzerland*

⊥*Equal contribution*

E-mail: anna.fontcuberta-morral@epfl.ch

1D Finite Element Simulations of Remote-Doping

1D finite element simulations were performed using the nextnano software package[S1] to simulate the band structure and carrier concentration of remotely-doped template-assisted nanowire (NW) structures. A simulation of a GaAs nanomembrane (NM) with either a pure InAs NW or intermixed $In_{0.5}Ga_{0.5}As$ NW on top was performed, as shown in Figure S1.

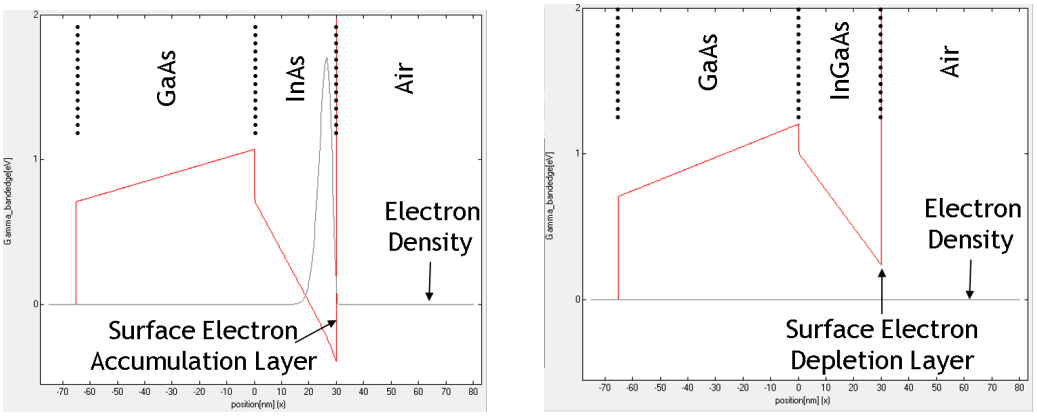

(a) Undoped InAs NW (b) Undoped $In_{0.5}Ga_{0.5}As$ NW

Figure S1: Finite element simulations showing the conduction band (red) and electron concentrations (grey) in undoped InAs (a) and $In_{0.5}Ga_{0.5}As$ (b) NWs.

Here, Fermi level pinning in the conduction band was assumed for the InAs NW, resulting in a large electron concentration near the surface of the NW. The Fermi level pinning was simulated by implementing a donor surface charge density of $2.5 \times 10^{12}\,\mathrm{cm}^{-2}$. In contrast, the InGaAs NW has no free electrons in the conduction band due to the lack of surface states which pin the Fermi level in the conduction band.

A 10 nm-thick modulation-doped layer was then inserted into the structure 20 nm below the InGaAs NW. A dopant concentration of $10^{19}\,\mathrm{cm}^{-3}$ was assumed. The result of this simulation is given in Figure S2.

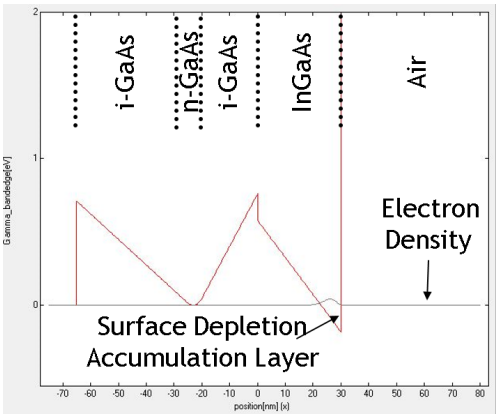

Figure S2: Finite element simulation of a modulation-doped $In_{0.5}Ga_{0.5}As$ NW showing the conduction band (red) and electron concentrations (gray). We see a maximum in the electron concentration now that appears in the InGaAs NW that appears due to the modulation-doped structure.

The addition of the remote doping layer does have an impact on the overall electron concentration in the NW. We now get a small peak in the electron density of $4 \times 10^{16}\,\mathrm{cm}^{-3}$. This basic 1D simulation was sufficient as a proof of concept, however, a more in-depth study was then performed using the NW structure as determined by scanning transmission electron microscopy (STEM) energy dispersive x-ray spectroscopy (EDS) investigations combined with atom probe tomography (APT), as described in the main text.

X-ray Fluorescence Mapping

To get a better understanding of the uniformity of the NWs, specifically in the Y-junction devices, x-ray fluorescence (XRF) mapping was performed at the European Synchrotron Radiation Facility (ESRF) by Jaime Segura-Ruiz. Figure S3 gives an example of two measurements performed on InGaAs Y-branch structures. We can see In K_α signal is relatively uniform across the junction for Figure S3a. However, in the opposite orientation shown in Figure S3b, both the scanning electron microscopy (SEM) image and the In K_α signal show a large degree of non-uniformity across the junction.

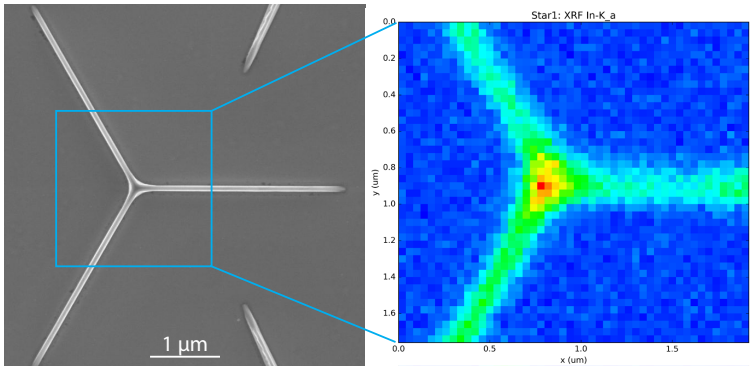

(a) Intersection of slits along $\langle \bar{1}\,\bar{1}\,2 \rangle$ directions.

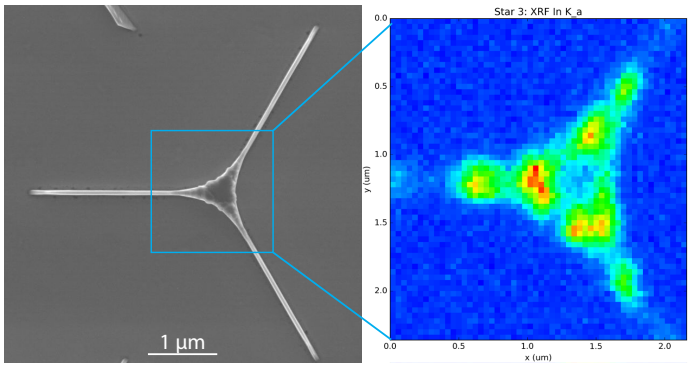

(b) Intersection of slits along $\langle 1\,1\,\bar{2} \rangle$ directions.

Figure S3: SEM images (left) combined with XRF maps of the In K_α signal (right) of InGaAs Y-branch structures in both the favourable intersection orientation (a) and unfavourable orientation (b).

The measurements were performed at the ID16B beamline at the ESRF with a beam size of 52 nm × 56 nm and beam energy of 29.8 keV.

Magnetoconductance Modeling

Here, we present the results from fitting the data with the clean limit as well as the diffusive limit. For clean limit, l_e was fixed at 20 nm to extract l_ϕ and l_{so}. The diffusive limit is valid when $l_e << W$. In this limit, the quantum correction to the classical conduction is given by

$$\Delta G = \frac{e^2}{h}\frac{1}{L}\left[3\left(\frac{1}{l_\phi^2}+\frac{4}{3l_{so}^2}+\frac{1}{l_B^2}\right)^{-1/2} - \left(\frac{1}{l_\phi^2}+\frac{1}{l_B^2}\right)^{-1/2}\right], \tag{1}$$

where here l_B is

$$l_B^2 = \frac{3\hbar^2}{e^2 W^2 B^2}. \tag{2}$$

Given that the mean free path of ~20 nm in the 3D regime is most appropriate, and our expected conducting channel's width is around this value, neither of the clean or the diffusive limits are exactly valid. The diffusive limit ignores boundary scattering completely, while the clean limit may over-emphasize this effect. Fits in the clean limit employing both specular as well as diffusive boundary scattering were conducted, giving very similar values for both. Next, we compare the diffusive fits to the clean fits, showing representative traces from both regimes below. From this plot, while both formulae give decent fits, we see that the clean regime fits the data slightly better than the diffusive regime, as evidenced by a smaller χ^2 in the fit (0.0025 vs 0.0081).

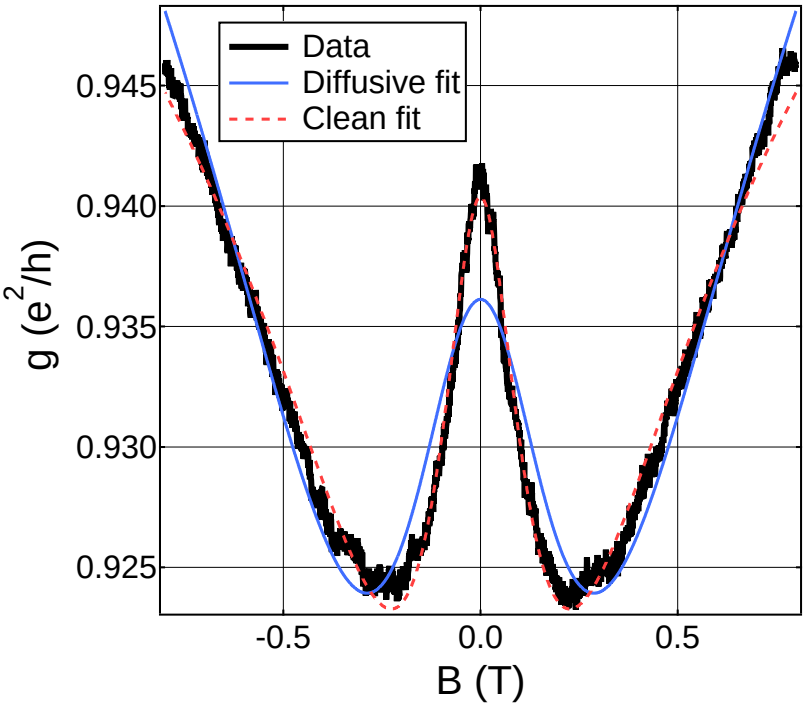

Figure S4: Comparison of magnetoconductance data fitting in the diffusive and clean limits. In the diffusive limit $l_\phi = 74$ nm and $l_{so} = 55$ nm, while in the clean limit $l_\phi = 94$ nm and $l_{so} = 70$ nm. Here we can see that the clean limit provides a much better fit to the experimental data.

Additional Magnetoconductance Measurements

The conduction of the device was also probed at 4 K and 1.9 K as a function of magnetic field and top gate voltage with and without the use of an AC oscillation coupled to the gate. First, we present the values for l_ϕ and l_{so} extracted using Equation (2) on the dataset in Figure 3 (d) of the main text (with AC coupling) in Figure S5. l_e was initially extracted as a fit parameter to Equation (1) of the main text and found to be 20 ± 5nm in the 3D limit. We then kept it fixed at 20 nm for the fits over the whole dataset. This was done to increase the reliability of the fits, as three free parameters are highly sensitive to starting conditions. Here, we find no significant change of l_{so} and l_ϕ as a function of V_g. Across the entire dataset l_ϕ has an average of 100 nm with a standard deviation of 10 nm and l_{so} 80 nm with standard deviation 5 nm.

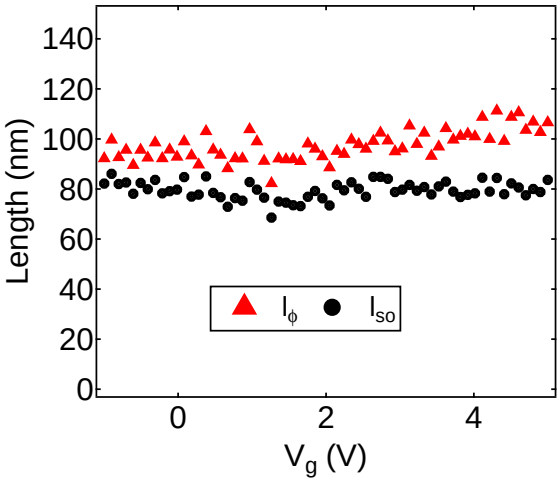

Figure S5: Plot of extracted values for l_ϕ and l_{so} from Figure 3 (d) of the main text. Data taken at 1.9 K.

In Figure S6, we present the results from unmodulated datasets taken at different temperatures on a different junction configuration compared to the previous data. The unmodulated data has a larger variance, but the overall trend of the values for l_ϕ and l_{so} remains the same. The agreement across multiple junction configurations is suggestive of a relatively homogeneous growth quality. The points are averages of traces taken at each particular value of gate

voltage, which were carried out to mitigate switchers in the some of magnetoconductance data, attributed to the presence of trapped charges in the HfO_2 dielectric layer.

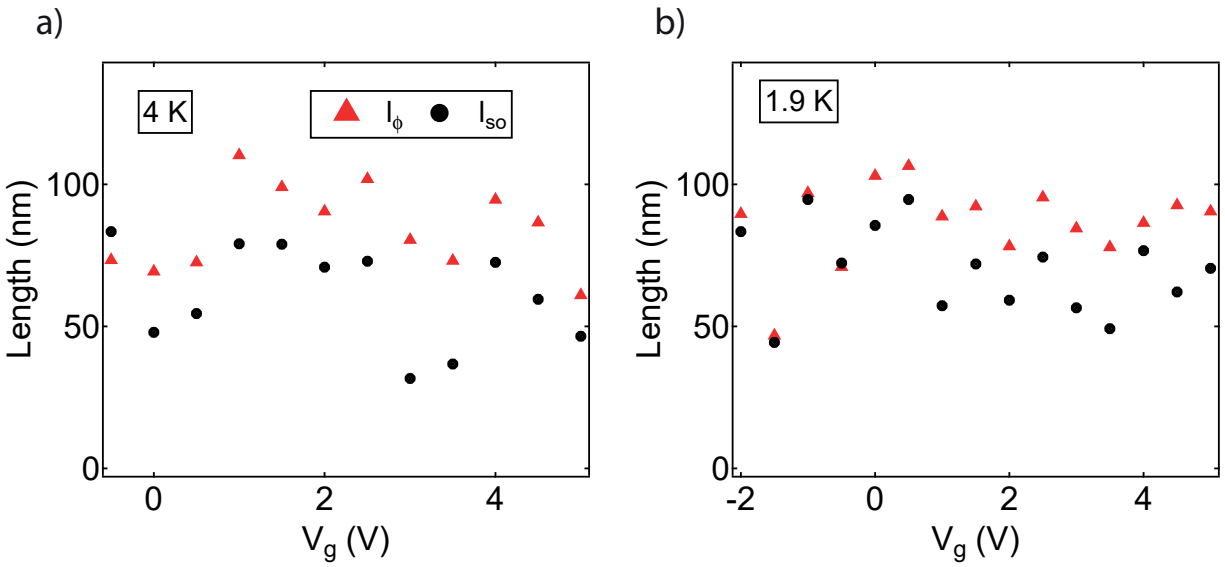

Figure S6: Plot of extracted values for l_ϕ and l_{so} at 4 K and 1.9 K (Figures (a) and (b) respectively) against gate voltage.

The analysis of the data, including the fitting, was carried out uniformly across the entirety of the data. It should be noted, however, that the weak anti-localization (WAL) formalism itself takes a uniform channel geometry into account, which is not the case across the junction. This introduces an additional uncertainty to the values of the extracted parameters (l_ϕ, l_{so}) through this formalism.

Description of Analysed Samples

Figure S7 depicts the main growth chip used for the APT and electrical analysis presented in this work. The growth chip consisted of a 1.2 cm triangle with three identical patterned regions labelled A, B and C. These regions were then used for various experiments. Region A was capped with HfO_2, yielded good electrical results and thus was kept for possible future experiments. Region B was also capped with HfO_2 for electrical experiments, however, high

resistances obscured any interesting transport properties. Instead, they were then processed for structural characterization for STEM and APT analysis. However, due to the HfO_2 not being a favourable capping layer for APT, Region C was exclusively dedicated to APT analysis. It was therefore capped by amorphous GaAs before performing APT on it.

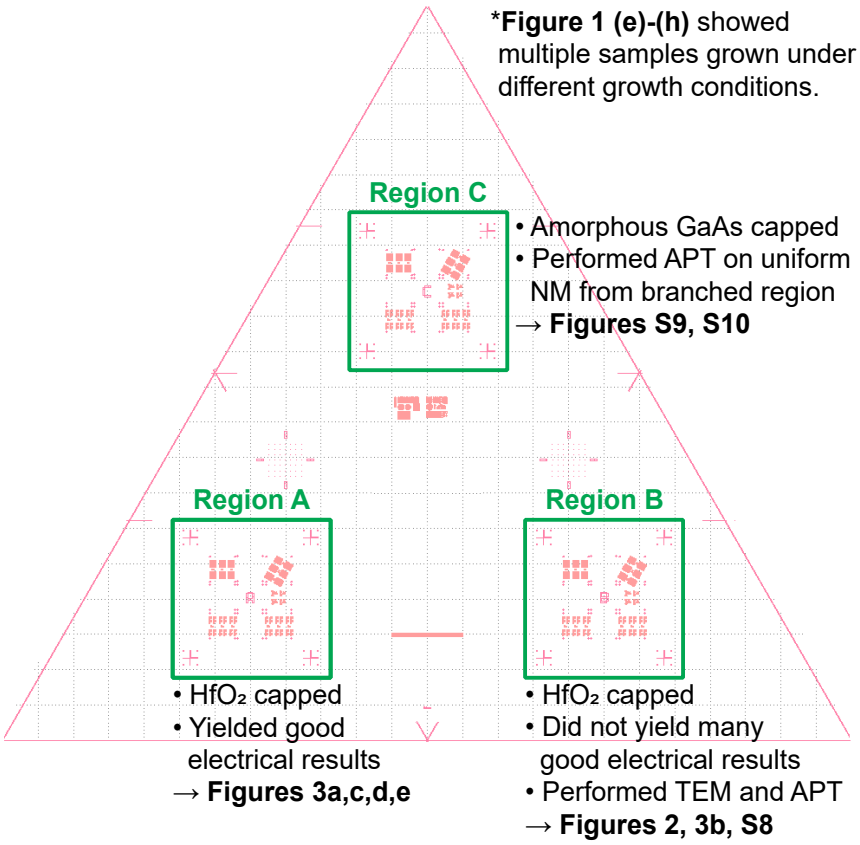

Figure S7: Diagram with descriptions of how the samples were processed for the structural and electrical analysis presented in this work.

APT analysis of multiple NWs from the same growth chip

APT analysis was carried out on three NWs from the same growth chip. Figure 2 shows analysis of the first nanowire, and Figure S8 shows mass spectra from isolated regions of this sample. Analysis of two additional nanowires is shown in Figure S9 and Figure S10. All samples exhibit a very similar Si distribution, i.e., the Si dopants are concentrated near

the InGaAs/GaAs interface. The peak at m/z=14 was found to be a reliable measure of the presence of Si dopants; m/z=14 was detected near the interface of each nanowire analyzed, but was not detected in measurable concentrations elsewhere. In contrast, the hit rate of m/z=28 was observed to increase in noisier regions at the beginning and end of the APT run, even in the absence of m/z=14, which likely indicates overlap with other species such as CO. For the sample in Figure 2, m/z=28 was closely correlated with m/z=14 in the region within 5-10 nm of the interface, so hits from both regions were included in Figure 2d. In Figure S9 and Figure S10, the species are plotted separately, with m/z=14 in grey and m/z=28 in light blue. The grey dashed line indicates the detection limit of Si^{++} and Si^{+} in these samples. Hits at m/z = 14.5, 15, 29 and 30, which include counts from $^{29}Si^{+}$, $^{30}Si^{++}$, $^{29}Si^{+}$, and $^{30}Si^{+}$, respectively, were not included in the analysis on concentration due to potential overlap with unidentified species. To correct for this systematic undercounting, concentrations based on ^{28}Si counts were multiplied by a factor of 1.084, which amounts to assuming a natural isotope abundance in the Si source.

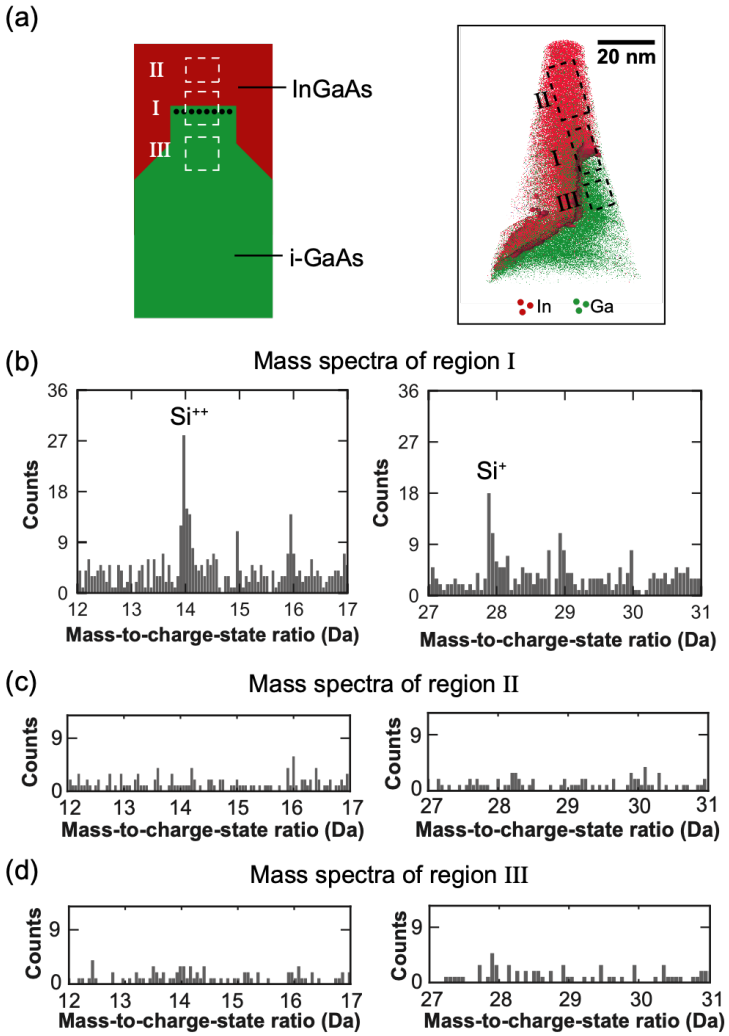

Figure S8: Mass spectra from different regions of the sample shown in Figure 2. (a) Schematic and corresponding APT reconstruction of the sample marked with the regions: (I) above the InGaAs/GaAs interface on the top; (II) around the top facet; (III) below the top facet. (b), (c), (d) Mass spectra near $^{14}Si^{++}$ and $^{28}Si^{++}$ in regions I, II, III respectively.

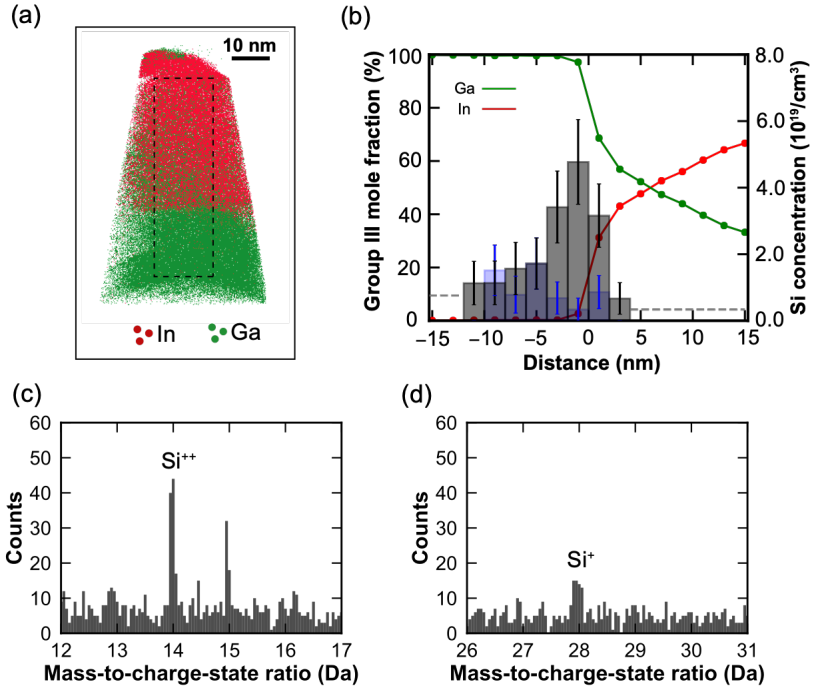

Figure S9: (a) APT reconstruction of a second sample. The black dashed line shows the region analyzed in the proxigram and mass spectra. (b) The proximity histogram of the sample moving from GaAs NM towards InGaAs NW. The distributions of Si^{++} and Si^{+} are shown in grey and light blue bars, respectively. The dashed grey line shows the detection limit of Si, which is sensitive to the total number of counts. (c), (d) Mass spectra around $^{14}Si^{++}$ and $^{28}Si^{++}$, respectively, for the region indicated by the black box in panel (a).

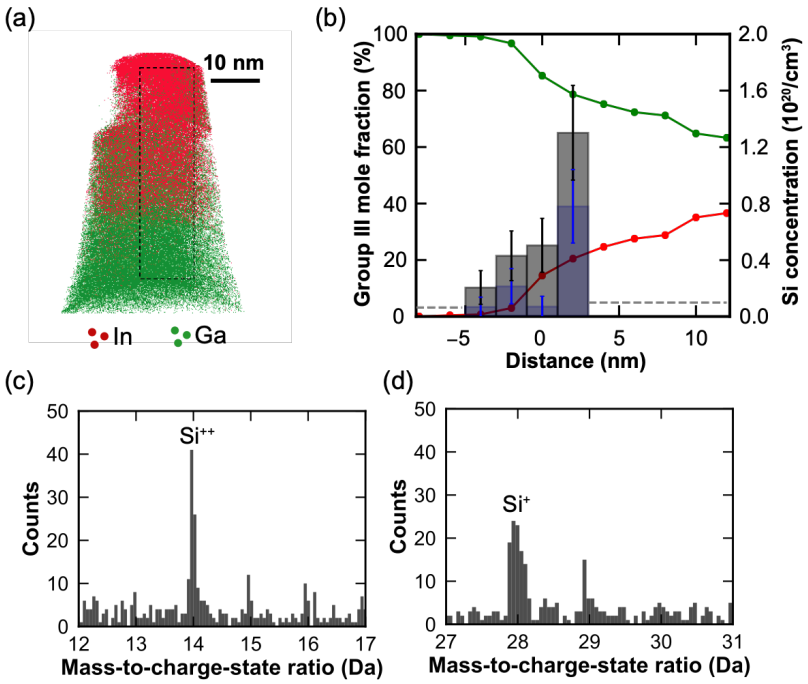

Figure S10: (a) APT reconstruction of a third sample. The black dashed line shows the region analyzed in the proxigram and mass spectra. (b) The proximity histogram of the sample moving from GaAs NM towards InGaAs NW. The distributions of Si^{++} and Si^{+} are shown in grey and light blue bars, respectively. The dashed grey line shows the detection limit of Si, which is sensitive to the total number of counts. (c), (d) Mass spectra around $^{14}Si^{++}$ and $^{28}Si^{++}$, respectively, for the region indicated by the black box in panel (a).

References

(S1) Birner, S.; Zibold, T.; Andlauer, T.; Kubis, T.; Sabathil, M.; Trellakis, A.; Vogl, P. nextnano: General Purpose 3-D Simulations. *IEEE Transactions on Electron Devices* **2007**, *54*, 2137–2142.